

# Application of Gaofen-5 Hyperspectral Data in Uranium Exploration: A Case Study of Weijing in Inner Mongolia, China

Yuantao Zhang (✉ [yuantao\\_zhang0606@163.com](mailto:yuantao_zhang0606@163.com))

Beijing Research Institute of Uranium Geology, National Key Laboratory of Science and Technology on Remote Sensing Information and Image Analysis, Beijing, China

**Wei Pan**

Beijing Research Institute of Uranium Geology, National Key Laboratory of Science and Technology on Remote Sensing Information and Image Analysis, Beijing, China

**Zhangfa Yu**

Beijing Research Institute of Uranium Geology, National Key Laboratory of Science and Technology on Remote Sensing Information and Image Analysis, Beijing, China

---

## Research Article

**Keywords:** Gaofen-5, AHSI, GLCM, matched filter

**Posted Date:** October 18th, 2021

**DOI:** <https://doi.org/10.21203/rs.3.rs-962878/v1>

**License:**   This work is licensed under a Creative Commons Attribution 4.0 International License.

[Read Full License](#)

---

# Abstract

Gaofen-5 (GF-5) satellite is the world's first full-spectrum hyperspectral satellite to achieve comprehensive observations of the atmosphere and land. The Advanced Hyperspectral Imager (AHSI) carried by GF-5 can acquire 330-channel imagery covering 390 - 2500 nm. However, the application of GF-5 AHSI imagery in uranium exploration is currently unknown. In this paper, the AHSI imagery was used for prospecting uranium mineralization in the Weijing, Inner Mongolia, China. The matched filter (MF) and threshold segmentation were used for mapping goethite, Al-high, Al-medium and Al-poor sericite. And the principal component analysis (PCA) and gray-level co-occurrence matrix (GLCM) were used to extract the texture information of the study area. Subsequently, combined with geological information, the relationship between alteration information, texture complexity and uranium mineralization was discussed, and it was pointed out that goethite, Al-medium, Al-poor sericite and texture complexity in this area can be used as indicators of uranium mineralization. Finally, three prospects were delineated, which will guide the follow-up uranium exploration in this area and promote the application of GF-5 AHSI data.

## Introduction

Hyperspectral remote sensing (HRS) began a revolution in remote sensing by combining traditional two-dimensional imaging remote sensing technology and spectroscopy, allowing for the synchronous acquisition of both images and spectra of objects<sup>[1]</sup>. And it has been extensively used in various fields such as geology, ecology, and agriculture<sup>[1,2]</sup>. And the application in geology is extremely extensive. Compared with multispectral imagery, more diagnostic absorption features of ground objects are recorded in hyperspectral imagery, so a number of studies based on these data have illustrated applications of structural interpretation<sup>[3,4]</sup>, mineral<sup>[4-10]</sup> and lithologic mapping<sup>[11-13]</sup>. Furthermore, from spectral characteristics, mineral chemistry, grain size<sup>[14]</sup> or the physical and chemical conditions of ore-forming fluids<sup>[15]</sup> can also be estimated.

Gaofen-5 satellite was successfully launched in May 2018. The visible and short-wave infrared hyperspectral camera onboard can simultaneously provides broad coverage and a broad spectrum, providing a new data source for surface research<sup>[13]</sup>. Currently, in terms of geological applications, a few researchers based on the AHSI imagery have performed structural interpretation<sup>[3]</sup>, lithology identification<sup>[3,13]</sup> and mineral extraction<sup>[16,17]</sup>. However, due to various reasons<sup>[16,17]</sup>, there are still few studies using this data to extract altered minerals, and there is no application in uranium exploration. Furthermore, most metallogenic predictions are based on the comprehensive analysis of the altered minerals, interpreted structures and other geological information extracted by remote sensing. If the texture information of the image was directly applied to the metallogenic prediction, it may avoid the complicated process of structure extraction, reduce the subjective influence of the interpreter and speed up the exploration progress.

Therefore, in order to promote the application of GF-5 hyperspectral data and the exploration of uranium in Weijing, Inner Mongolia, China, we used the typical mineral mapping process, including Minimum Noise Fraction (MNF), Pixel Purity Index (PPI), N-dimensional visualization and mineral mapping techniques<sup>[5]</sup>, to map alteration minerals, and used GLCM to extract texture complexity. Finally, through a comprehensive analysis of alteration minerals, texture complexity and geological data, three prospects have been delineated.

**Geologic Setting.** The study area located on the border of China and Mongolia in the southwest of Erliaohot is hilly grassland area, with exposed bedrock and relatively flat terrain. It is located in the southwestern section of Bayinbaolige uplift and at the border between the southern margin of the Siberian plate and the northern margin of the North China Block<sup>[18]</sup>. The major exposed strata in the region consist of Qingbaikou System, Dashizhai Group in Early Permian, Late Jurassic System, Late Cretaceous System, Neogene and Quaternary System. The Qingbaikou System is mainly a set of metamorphic rocks including marble, schist, slate and crystalline limestone. The Dashizhai Group, including the First, Second, Third and Fourth Formations, is mainly composed of phyllite, tuff, rhyolite, slate, marble and dacite. The main lithology of the Second Formation of Manketou Obo Group in Late Jurassic includes tuff, volcanic breccia and pebbly sandstone. The lithology of the Late Cretaceous system is composed mainly of mudstone, sandstone and glutenite. And the dominant lithology of the Neogene System is a set of sedimentary rocks, including mudstone and glutenite. Furthermore, the intrusive rocks are widespread in this area, mainly including Late Permian monzogranite, Early Cretaceous granite, Early Jurassic granite and Early Jurassic monzogranite. Locally, there are Late Jurassic granite, Late Permian granite, Early Permian diorite and Silurian granite (Fig. 1).

**GF-5 AHSI imagery.** GF-5 is the fifth satellite of a series of the China High-Resolution Earth Observation System (CHEOS) satellites of the China National Space Administration (CNSA), which can achieve high spectral resolution observations<sup>[13]</sup>. It is equipped with six payloads, including visible and short-wave infrared hyper-spectral camera (AHSI), spectral imager, greenhouse gas detector, atmospheric environment infrared detector at very high spectral resolution, differential absorption spectrometer for atmospheric trace gas, and multi-angle polarization detector. Among them, AHSI can acquire a total of 330 bands including Visible/Near-infrared (VNIR) and Shortwave infrared (SWIR) data, and the swath width of the imagery is up to 60 km. Table 1 shows the waveband setting and spatial resolution of the GF-5 AHSI imagery. The AHSI imagery downloaded from the High-resolution Earth observation system grid platform (<https://www.cheosgrid.org.cn/index.htm>) was acquired on November 3, 2019, and its scene number and data level are 88317 and L1 respectively. In addition, the imagery is clear without interference from clouds and snow.

**Table 1.** Major parameters of Gaofen-5 AHSI imagery

Band	Spectral range (nm)	Spectral resolution (nm)	Spatial resolution (m)	Bands
VNIR	390.324-1029.18	5	30	150
SWIR	1004.77-2513.25	10		180

## Methods

Varying atmospheric conditions, differences in the sun geometry, topographic effects and the sensor scanning system strongly influence the recorded signal. And these influences modify the true spectrum of the ground features, Which means that the original data cannot be used quantitatively<sup>[2]</sup>. Therefore, to obtain the real spectrum of the ground objects from imagery and carry out alteration extraction, preprocessing such as radiometric calibration, accurate atmospheric correction and geometric correction must be performed. After image preprocessing, the typical mineral mapping process, including Minimum Noise Fraction (MNF), Pixel Purity Index (PPI), N-dimensional visualization and mineral mapping techniques, was used to extract alteration information in 400-1000 nm and 2058-2361 nm range respectively. Additionally, PCA and GLCM were used to extract texture information in the study area. The detailed methodology flowchart is shown in Fig. 2.

**Hyperspectral image processing.** The preprocessing of GF-5 AHSI imagery mainly included radiometric calibration, atmospheric correction, band selection, destriping, orthorectification and spectral denoising.

(1) Radiometric calibration. It includes relative calibration and absolute calibration. The relative calibration is used to remove the effects of the non-uniformity of the detector response. The absolute radiometric calibration is used to convert the detector response digital number (DN) values to radiance received by the optical aperture<sup>[2]</sup>. In this paper, the Radiometric Calibration tool from ENVI (Environment for Visualizing Images) software version 5.3 was used to calibrate AHSI data. During processing, band interleaved by line (BIL) and scale factor of 0.1 were adopted.

(2) Atmospheric Correction. Gas molecules and aerosols in the atmosphere absorb and transmit the incoming light in regards to its wavelength and this causes distortions in the image. To eliminate the influence of atmosphere in the image, an atmospheric correction is necessary in which the raw radiance image is converted to a reflectance image. In this paper the Fast Line-of-sight Atmospheric Analysis of Spectral Hypercubes (FLAASH) atmospheric correction model from ENVI software version 5.3 was adopted. The FLAASH model is based on the MODTRAN radiative transfer model and is widely used in hyperspectral<sup>[12,13]</sup> and multispectral imagery<sup>[19]</sup>. During the correction process, Tiled Processing was not performed.

(3) Band selection. To obtain well results, the bands without calibration, contaminated by strips and overlapped between VNIR (1006.68-1028.98nm) and SWIR (1004.57-1029.85 nm) were removed<sup>[20]</sup>. Additionally, considering the difference of the diagnostic spectral characteristics of anions and cations, we selected the data from 400-1000 nm and 2058-2361 nm respectively.

(4) Destriping. The problems of stray light interference, slit contamination, and instrument instability caused stripe noise<sup>[2]</sup>. To remove the obvious vertical stripes, the global destriping method<sup>[21]</sup> was adopted. After processing, the vertical stripes of the image can be effectively eliminated (Fig. 3).

(5) Orthorectification. Orthorectification, as the highest level of geometric correction, can simultaneously remove the effects of image **perspective** and **relief** effects for the purpose of creating a planimetrically correct image. After correction, the AHSI imagery was georeferenced to a UTM projection using the WGS-84 datum (UTM zone 49N).

(6) Spectral denoising. To improve the signal to noise ratio (SNR), The first 15 Minimum Noise Fraction (MNF) bands were selected for inverse MNF rotation. MNF rotation can be used to judge the intrinsic dimension of imagery data, separate noise, and reduce the demand for processing and calculation<sup>[22]</sup>, which is extensively used in hyperspectral research.

**Alteration mineral mapping.** Alteration mineral mapping is one of the main research contents of HRS, which has been extensively studied<sup>[2,4-10,23,24]</sup>. In general, the diagnostic absorption features of anions are mainly located in the 2000-2500 nm range, and the diagnostic absorption features of  $\text{Fe}^{2+}$ ,  $\text{Fe}^{3+}$  and  $\text{Mn}^{2+}$  are mainly located in the 400-1200 nm range<sup>[25,26]</sup>. Therefore, The data of two spectral range was used to extract the altered minerals respectively. The typical mineral mapping process is the earliest technique for hyperspectral information extraction and has been extensively used in mineral mapping<sup>[5,9,27,28]</sup>, which is implemented in the ENVI software.

After MNF, PPI and n-dimensional visualizer processing, the endmembers of the VNIR and SWIR spectral range were extracted respectively. A total of five endmember spectra were obtained in the VNIR spectral range. To identify these spectra, the Spectral Analyst model in ENVI software was used by comparing their spectral signatures with these from the USGS spectral library. Additionally, expert knowledge was also adopted to comprehensively analyze the characteristic absorption position, absorption depth, absorption width and overall shape of each endmember spectrum. After that, one goethite spectrum was finally identified in the VNIR spectral range, which is highly consistency with the USGS reference spectrum on waveform and absorption position (Fig. 4(a)). In the SWIR region, A total of seven endmember spectra were obtained, and the characteristic absorption position, absorption depth, absorption width, waveform and the analysis results from the Spectral Analyst model were comprehensively considered. Finally, four altered mineral endmembers were obtained. Among them, there are two endmember spectra that are similar in waveform, characteristic absorption position and absorption depth. Therefore, These two endmember spectra were merged.

Numerous studies have shown that the aluminum hydroxyl (Al-OH) absorption of sericite (white mica) near 2200 nm can be used to estimate its  $\text{Al}^{\text{VI}}$  content<sup>[15,29-33]</sup>. And the absorption position varies from 2190 nm to 2225 nm<sup>[34]</sup>, which can be used to distinguish Al-poor, Al-medium and Al-high sericite<sup>[15,16]</sup>. However, there is still no consistent metric for distinguishing different aluminum content sericite (white mica). For instance, some researchers distinguished long wavelength micas and short wavelength micas

with 2220 nm as the boundary<sup>[33]</sup>. However, some researchers used the primary absorption characteristic of Al-OH at 2195 nm, 2210 nm and 2225 nm in combination with the common secondary absorption characteristic at 2345 nm to identify Al-high, Al-medium, and Al-poor sericite respectively<sup>[15]</sup>. In this paper, the three endmembers in the SWIR region have common secondary absorption characteristic near 2345 nm, and the main absorption characteristic appearing at 2201 nm, 2210 nm, and 2218 nm, respectively. Based on it, the Al-high, Al-medium and Al-poor sericite are identified (Fig. 4(b)).

Mineral mapping is one of the ultimate aim of the utilization of hyperspectral data in mineral exploration<sup>[8]</sup>. After acquiring and identifying the endmember spectra, the mapping algorithm can be used to analyze the relationship between the reference spectra and image spectra, so as to achieve alteration mineral mapping and inversion of their abundance. Mapping algorithms can be subdivided broadly into per pixel and subpixel methods<sup>[8]</sup>. Among them, pixel-based spectral angle matching (SAM) and spectral information divergence (SID), and subpixel-based hybrid modulation matched filtering (MTMF) and matched filtering (MF) algorithms have been extensively applied. MF is a partial unmixing or spectral decomposition technique to find the abundances of target(s) of interest in each pixel of a hyperspectral image, which can maximize the response of the target of interest and suppress the response of the compound unknown background<sup>[8]</sup>. And the output is the matched filter score. The closer the score is to 1, the better the pixel spectrum matches the reference spectrum<sup>[35]</sup>.

Threshold segmentation is commonly used to separate and extract the anomalous information by intensity. In this study, The threshold values of MF outputs were mean + 2 (standard deviation). Additionally, a median filtering with 3 × 3 pixels window was applied to remove isolated anomalous pixels and optimize the segmentation results.

**Texture information extraction.** Texture is an important image spatial feature, which refers to the frequency of tonal change in an image<sup>[36]</sup>. Surface rocks show specific textures on the image due to the combined effect of internal minerals and structures, as well as external geological structures, weathering and denudation. The author believes that the texture in the area with less artificialities mainly reflects the information such as geological structure and lithology, including faults, joints, veins, rock bedding and contact plane. Therefore, the direct use of texture information instead of geological structures may improve work efficiency, while partly avoiding the influence of subjectivity during visual interpretation of geological structures. Additionally, compared to automatic recognition of geological structures, it can retain more original information.

Many texture descriptors have been developed in the past, and the gray-level co-occurrence matrix (GLCM) is the most commonly implemented. GLCM provides information in image gray direction, interval and change amplitude, so that 14 kinds of texture features can be effectively defined based on it<sup>[37]</sup>. In this paper, based on the PC 1 obtained from PCA of VNIR data (400-1000 nm) and the GLCM with 3 × 3 pixels window, the contrast textural measure was calculated from four directions of 0°, 45°, 90° and 135°, respectively. And the final texture image of the study area was calculated by the average operation. To obtain texture complexity, the texture image was first converted to a binary image by the threshold value

selected by the interpreter by observing arbitrary transects on the texture image. And then the texture complexity was generated by converting raster to point, deleting zero-value points and generating point density in ArcGIS software.

## Results

**Mapping of alteration minerals.** The typical mineral mapping process was used to map goethite, Al-high sericite, Al-medium sericite, and Al-poor sericite from VNIR and SWIR region respectively. The result shows that goethite mainly concentrates in the Chaganhada in the northwest of the study area, showing clump distribution; Al-high sericite is mainly distributed in the Cretaceous and Permian igneous intrusions in the form of clump and star point; Al-medium sericite is mainly exposed in the southeast, middle and northwest of the study area in the form of clump, band and star point. Especially in the southeast, its distribution is wide and consistent with the strata. Moreover, there is a anti-y-shaped alteration zone in the middle area; And for Al-poor sericite, it mainly distributes in the strata in the south and southeast, showing clump and star point distribution (Fig. 5).

**Extraction of texture complexity.** The texture complexity of the study area was obtained using GLCM and ArcGIS software. The redder the color in the image is, the more complex the texture of the corresponding area is. The result shows that the complex texture areas are mainly distributed in the southeast, middle and northwest. In general, areas with complex texture mostly appear in the strata outside the igneous intrusions (Fig. 6).

## Discussion

**The reflection of texture information on lithology and structure.** Texture information is one of the important information of remote sensing image. The spatial features of the surface rock unit are controlled by the microtopography such as structures, combination features, outcropping state and distribution of surface gullies, which show different aggregate texture graphics<sup>[38]</sup>. Therefore, these texture features can truthfully describe the geological information such as geological structures, lithological boundaries and lithology in the area with less artificialities<sup>[39]</sup>. This can be reflected in the fact that supplementary texture information can effectively improve the accuracy of lithology classification<sup>[38,40,41]</sup>. Additionally, texture information is also one of the basis of structure interpretation, which can be validated in Figure 7. These areas with higher texture complexity are distributed in NW-trending strips, which are closely related to the NW-trending valleys that are obviously controlled by geological structures (Fig. 7). Thus, to fully and accurately extract the geological structure, texture enhancement is applied in many applications<sup>[42-44]</sup>. In short, the texture information extracted in this paper contains not only geological structure information such as faults, joints, and veins, but also lithological information such as rock bedding and rock contact planes. And it can be regarded as crack information, which provides a favorable space for the migration of hydrothermal fluid and mineralization.

**Mineralization prediction.** The metallogenic information such as radioactive anomalies and uranium mineralization points found in the study area was superimposed on alteration minerals and texture complexity extracted above (Figs. 5, 6). From the perspective of distribution of alteration minerals, in the Chaganha, goethite is distributed widely, and Al-high, Al-medium and Al-poor sericites are also found locally, which indicates that the uranium mineralization in this place is closely related to the four types of alteration minerals, especially goethite; In the Tuiraomuchagan Obo, these four alteration minerals are not obvious. However, our previous field work found an ~EW-trending alteration zone controlled by a fault, with strong silicification, hematite, limonite and kaolinization<sup>[45]</sup>. It may be due to the limitation of the low spatial resolution of AHSI imagery, which results in failure to extract the small-scale alteration anomaly; In the anti-y-shaped alteration zone in the middle of the study area, our previous study has shown that Al-OH, Mg-OH, Fe-OH, and CO<sub>3</sub><sup>2-</sup>-bearing alteration minerals are widely distributed and the silicidation alteration intensity is high<sup>[45]</sup>. And this study found that the Al-OH-bearing alteration minerals in the anti-y-shaped area zone are mainly Al-medium sericites, which are surrounded by Al-poor sericites; In the southeast of the study area, our previous studies have pointed out that Al-OH-bearing altered minerals are the most developed<sup>[46,47]</sup>. This study found that the Al-OH-bearing alteration minerals developed in the contact zone between granite and wall rock are mainly Al-medium sericites (Fig. 5). For texture complexity, the texture complexity of the favorable uranium mineralization areas is relatively high except for the Tuiraomuchagan Obo area (Fig. 6). Therefore, ignoring the constraints of the low spatial resolution, the areas with complex texture reveal the well developed cracks which may contribute to the flow and accumulation of hydrothermal fluid.

In summary, goethite, Al-medium sericite, Al-poor sericite and texture complexity can be used as vectors to mineral deposit exploration in this area. Based on these, three prospects (area I, II, III) were identified. Among them, Prospect I is close to the favorable metallogenic section of Chaganhada, with contiguous goethite and high texture complexity; Prospect II is close to the favorable mineralization section in the southeast of the study area, with densely distributed Al-medium sericites, Al-poor sericites and goethite; Prospect III is located in the southern section of the study area, and two radioactive anomalies have been found nearby. The band characteristics of the Al-medium and Al-poor sericites are obvious, showing significant characteristics controlled by the geological structures. Moreover, the texture complexity is also high (Figs. 5, 6).

## Conclusion

Based on GF-5 AHSI data, this research performed mineral mapping, texture information extraction, and uranium mineralization prediction in Weijing, Inner Mongolia, China. The typical mineral mapping process was successfully used to extract the alteration minerals including goethite, Al-poor, Al-medium and Al-high sericite in the study area. The GLCM was adopted to extract the image texture information, and the texture complexity map was made. Furthermore, the relationship between the extracted texture and geological structure and lithology was analysed. And the texture information is a reflection of the fracture planes in the study area, which can facilitate the migration and accumulation of hydrothermal fluids.

After that, The goethite, Al-medium and Al-poor sericite, as well as texture complexity were used as the indicative elements for uranium exploration in this area. Finally, three prospects have been delineated, which will provide guidance for subsequent uranium exploration in this area and also provide a reference for the geological application of GF-5 AHSI data.

## Declarations

### Acknowledgments

This study was financially supported by the Concentrated Research Development Project of the China National Nuclear Corporation (Research on new technology and integration of sandstone-type uranium deposit detection), and the State Administration of Science, Technology and Industry for National Defence (High-resolution remote sensing data (civilian part) in uranium resources exploration and verification application, Grant No. GF1701). We would like to express our gratitude to the earth observation and data center of CNSA for providing the Gaofen-5 AHSI imagery.

### Author contributions

Y.Z. and W.P. and Z.Y. were involved equally in designing the study, analyzing the data, and writing the manuscript. All authors reviewed the manuscript.

### Competing interests

The authors declare no competing interests.

## References

1. Tong, Q., Xue, Y. & Zhang, L. Progress in hyperspectral remote sensing science and technology in China over the past three decades. *IEEE J-Stars*, **7** (1), 70–91 (2013).
2. Jia, J. *et al.* Status and application of advanced airborne hyperspectral imaging technology: A review. *Infrared Phys. Techn*, **104**, 103115 (2020).
3. Li, N. *et al.* Preliminary application and evaluation of GF-5 satellite hyperspectral data in lithology-structure interpretation. *Aerospace Shanghai (In Chinese)*, **36** (S2), 187–198 (2019).
4. Liu, D., Qiu, J., Tian, F. & Yu, S. Application of airborne hyper-spectrum remote sensing to mapping of ore-control faults: A case study of the Heishishan-Huaniushan fault. *Geology and Exploration (In Chinese)*, **51** (2), 366–375 (2015).
5. Kruse, F. A. Integrated visible and near-infrared, shortwave infrared, and longwave infrared full-range hyperspectral data analysis for geologic mapping. *J. Appl. Remote Sens*, **9** (1), 096005 (2015).
6. Liu, L. *et al.* Mapping alteration using imagery from the Tiangong-1 hyperspectral spaceborne system: Example for the Jintanzi gold province, China. *Int. J. Appl. Earth Obs*, **64**, 275–286 (2018).

7. Zhang, C. *et al.* Three-dimensional modeling of alteration information with hyperspectral core imaging and application to uranium exploration in the Heyuanbei uranium deposit, Xiangshan, Jiangxi, China. *J. Appl. Remote Sens*, **13** (1), 014524 (2019).
8. Guha, A. Mineral exploration using hyperspectral data. *Hyperspectral Remote Sensing. Elsevier*, 293–318 (2020).
9. Tripathi, M. K., Govil, H. & Chatteraj, S. L. Identification of hydrothermal altered/ weathered and clay minerals through airborne AVIRIS-NG hyperspectral data in Jahajpur, India. *Heliyon* 6(2), e03487 (2020).
10. Govil, H., Mishra, G., Gill, N., Taloor, A. & Diwan, P. Mapping hydrothermally altered minerals and gossans using hyperspectral data in Eastern Kumaon Himalaya, India. *Applied Computing and Geosciences*, **9**, 100054 (2021).
11. Zhang, X. & Li, P. Lithological mapping from hyperspectral data by improved use of spectral angle mapper. *Int. J. Appl. Earth Obs*, **31**, 95–109 (2014).
12. Kumar, C., Chatterjee, S., Oommen, T. & Guha, A. Automated lithological mapping by integrating spectral enhancement techniques and machine learning algorithms using AVIRIS-NG hyperspectral data in Gold-bearing granite-greenstone rocks in Hutti, India. *Int. J. Appl. Earth Obs*, **86**, 102006 (2020).
13. Ye, B., Tian, S., Cheng, Q. & Ge, Y. Application of Lithological Mapping Based on Advanced Hyperspectral Imager (AHSI) Imagery Onboard Gaofen-5 (GF-5) Satellite. *Remote Sens*, **12** (23), 3990 (2020).
14. Lypaczewski, P. *et al.* Characterization of Mineralogy in the Highland Valley Porphyry Cu District Using Hyperspectral Imaging, and Potential Applications. *Minerals*, **10** (5), 473 (2020).
15. Ye, F. *et al.* Minerageny study of high-Al, medium-Al and low-Al sericites identified by airborne hyperspectral remote sensing technology. *Acta Geologica Sinica (In Chinese)*, **92** (2), 395–412 (2018).
16. Dong, X. F. *et al.* Fine mineral identification of GF-5 hyperspectral image. *Journal of remote sensing (In Chinese)*, **24** (4), 454–464 (2020).
17. Lian, C., Yao, F., Chen, M., Ma, K. & Wang, H. The study on alteration information extraction of GF-5 hyperspectral data in vegetation coverage area: A case study of the Yushui Copper Deposit in Guangdong Province. *Geoscience (in Chinese)*, **34** (4), 680–686 (2020).
18. Xiao, W., Windley, B. F., Hao, J. & Zhai, M. Accretion leading to collision and the Permian Solonker suture, Inner Mongolia, China: Termination of the central Asian orogenic belt. *Tectonics* **22**(6) (2003).
19. Sun, Y., Tian, S. & Di, B. Extracting mineral alteration information using WorldView-3 data. *Geosci. Front*, **8** (5), 1051–1062 (2017).
20. Wan, L. *et al.* GF-5 hyperspectral data for species mapping of mangrove in Mai Po, Hong Kong. *Remote Sens*, **12** (4), 656 (2020).
21. Tian, B., Li, Z., Chen, E. & Pan, Y. Preprocessing of EO-1 Hyperion hyperspectral data. *Remote Sensing Information (In Chinese)*(6), 36–41 (2005).

22. Green, A. A., Berman, M., Switzer, P. & Craig, M. D. A transformation for ordering multispectral data in terms of image quality with implications for noise removal. *IEEE Trans. Geosci. Remote Sens*, **26** (1), 65–74 (1988).
23. Van der Meer, F. D. *et al.* Multi-and hyperspectral geologic remote sensing: A review. *Int. J. Appl. Earth Obs*, **14** (1), 112–128 (2012).
24. Portela, B., Sepp, M. D., van Ruitenbeek, F. J., Hecker, C. & Dilles, J. H. Using hyperspectral imagery for identification of pyrophyllite-muscovite intergrowths and alunite in the shallow epithermal environment of the Yerington porphyry copper district. *Ore Geol. Rev*, **131**, 1–14 (2021).
25. Gan, F., Wang, R., Ma, A., Zhang, Z. & Li, M. Integration for extracting and mineral analysis models for geological application using remote sensing data. *Journal of remote sensing (In Chinese)*, **7** (3), 207–214 (2003).
26. Peyghambari, S. & Zhang, Y. Hyperspectral remote sensing in lithological mapping, mineral exploration, and environmental geology: an updated review. *J. Appl. Remote Sens*, **15** (3), 031501 (2021).
27. Tripathi, M. K. & Govil, H. Evaluation of AVIRIS-NG hyperspectral images for mineral identification and mapping. *Heliyon*, **5** (11), e02931 (2019).
28. Fan, Y. *et al.* Application of an airborne hyper-spectral survey system CASI/SASI in the gold-silver-lead-zinc ore district of Huaniushan, Gansu, China. *Geol. Croat*, **74** (1), 73–83 (2021).
29. Lypaczewski, P. *et al.* Using hyperspectral imaging to vector towards mineralization at the Canadian Malartic gold deposit, Québec, Canada. *Ore Geol. Rev*, **111**, 102945 (2019).
30. Post, J. L. & Noble, P. N. The near-infrared combination band frequencies of dioctahedral smectites, micas, and illites. *Clay Clay Miner*, **41** (6), 639–644 (1993).
31. Duke, E. F. Near infrared spectra of muscovite, Tschermak substitution, and metamorphic reaction progress: Implications for remote sensing. *Geology* **22**(7), 621–624 (1994).
32. Van Der Meer, F. Analysis of spectral absorption features in hyperspectral imagery. *Int. J. Appl. Earth Obs*, **5** (1), 55–68 (2004).
33. Wang, R. *et al.* White mica as a hyperspectral tool in exploration for the Sunrise Dam and Kanowna Belle gold deposits, Western Australia. *Econ. Geol*, **112** (5), 1153–1176 (2017).
34. Zhang, C., Ye, F., Wang, J., Qiu, J. & Meng, S. Spectral characteristics analysis of drill core in the Xiangyangping Uranium Deposit in the Middle Miaoershan Mountain, Northeastern Guangxi. *Uranium Geology (In Chinese)*, **35** (6), 366–272 (2019).
35. Salehi, T. & Tangestani, M. H. Large-scale mapping of iron oxide and hydroxide minerals of Zefreh porphyry copper deposit, using Worldview-3 VNIR data in the Northeastern Isfahan. *Iran. Int. J. Appl. Earth Obs*, **73**, 156–169 (2018).
36. Kiefer, R. W., Lillesand, T. M. & Chipman, J. W. *Remote Sensing and Image Interpretation* 6th edn (John Wiley & Sons, Hoboken, NJ, 2008).

37. Haralick, R. M., Shanmugam, K. & Dinstein, I. H. Textural features for image classification. *IEEE Trans, Syst. Man Cybern.* **3** (6), 610–621 (1973).
38. Zhang, C., Yu, J., Hao, L. & Wang, S. Lithology extraction from synergies multi-scale texture and multi-spectra images. *Geological Science and Technology Information (In Chinese)*, **36** (4), 1844–1854 (2017).
39. Huang, Y., Li, P. & Li, Z. The application of geostatistical image texture to remote sensing lithological classification. *Remote Sens. Land Resour. (In Chinese)*(3),45–49(2003).
40. Chica-Olmo, M. & Abarca-Hernandez, F. Computing geostatistical image texture for remotely sensed data classification. *Comput. Geosci*, **26** (4), 373–383 (2000).
41. Li, P., Li, Z. & Moon, W. M. Lithological discrimination of Altun area in northwest China using Landsat TM data and geostatistical textural information. *Geosci J*, **5** (4), 293–300 (2001).
42. Hamdani, N. & Baali, A. Fracture network mapping using Landsat 8 OLI data and linkage with the karst system: a case study of the Moroccan Central Middle Atlas. *Remote Sens. Earth Syst. Sci*, **2** (1), 1–17 (2019).
43. Javhar, A. *et al.* Comparison of multi-resolution optical Landsat-8, Sentinel-2 and radar Sentinel-1 data for automatic lineament extraction: A case study of Alichur area, SE Pamir. *Remote Sens*, **11** (7), 778 (2019).
44. Farahbakhsh, E. *et al.* Computer vision-based framework for extracting tectonic lineaments from optical remote sensing data. *Int. J. Remote Sens*, **41** (5), 1760–1787 (2020).
45. Zhang, Y., Yu, Z., Pan, W. & Tian, Q. Application of WorldView-3 and ASTER TIR for the exploration of uranium in Weijing, Inner Mongolia. *Uranium Geology (In Chinese)*, **36** (5), 408–417 (2020).
46. Yu, Z., Pan, W., Zhang, Y., Li, H. & Tian, Q. Application of remote sensing technique to uranium exploration in Sumoqagan Obo District, Inner Mongolia. *Uranium Geology (In Chinese)*, **34** (6), 372–378 (2018).
47. Zhang, Y., Pan, W., Yu, Z. & Tian, Q. Application of WorldView-3 image in uranium exploration in Sumoqagan Obo, Inner Mongolia. *Uranium Geology (In Chinese)*, **35** (2), 130–137 (2019).

## Figures

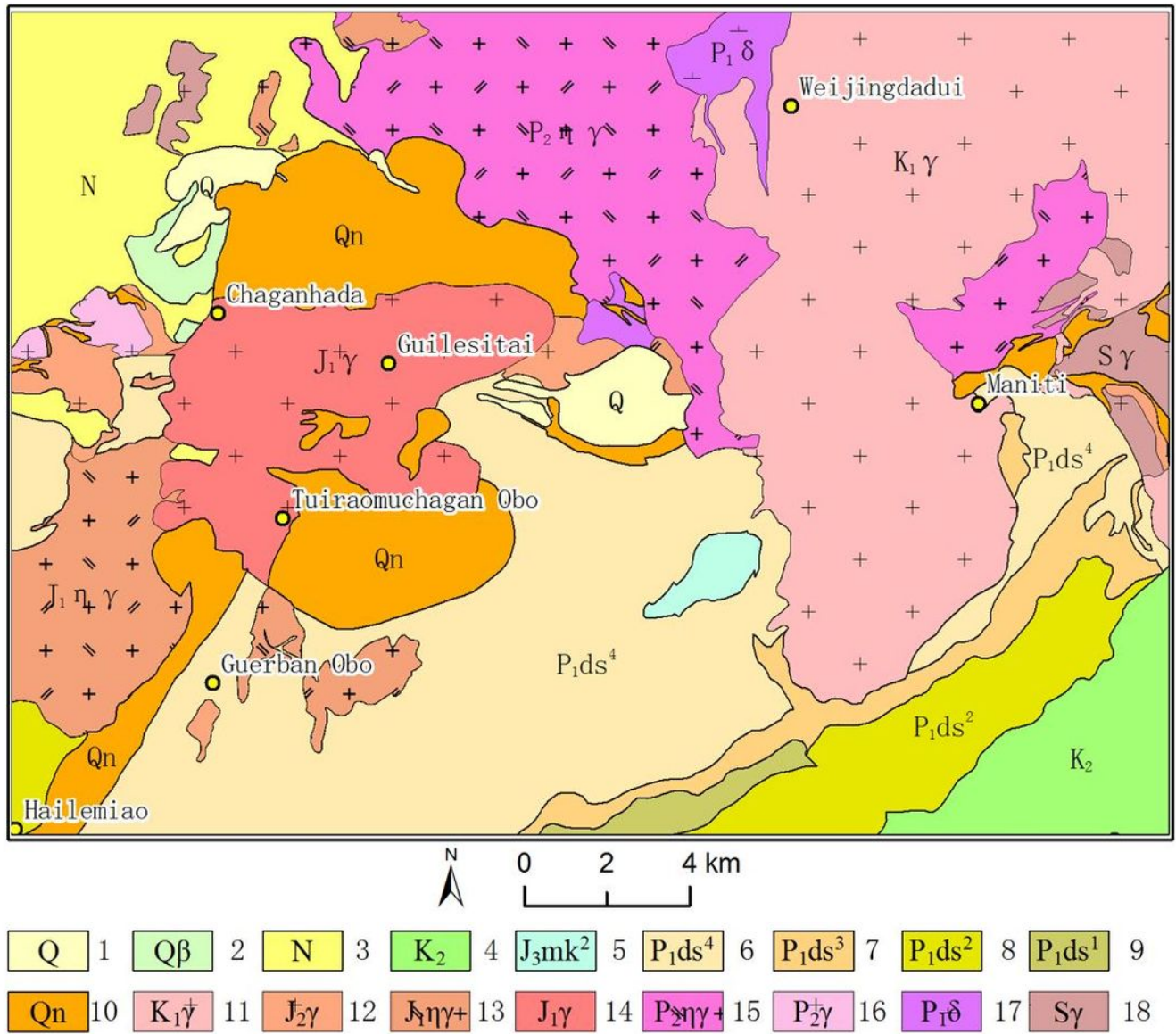


**Figure 1**

Sketch geological map of research area. 1. Quaternary; 2. Basalt; 3. Neogene; 4. Cretaceous; 5. The Second Formation of Manketou Obo Group in Late Jurassic; 6. The Fourth Formation of Dashizhai Group in Early Permian; 7. The Third Formation of Dashizhai Group in Early Permian; 8. The Second Formation of Dashizhai Group in Early Permian; 9. The First Formation of Dashizhai Group in Early Permian; 10. Qingbaikou System; 11. Early Cretaceous granite; 12. Late Jurassic granite; 13. Early Jurassic monzogranite; 14. Early Jurassic granite; 15. Late Permian monzogranite; 16. Late Permian granite; 17. Early Permian diorite; 18. Silurian granite. This map was created in ESRI ArcMap 10.2 (<https://desktop.arcgis.com/zh-cn/arcmap/>).

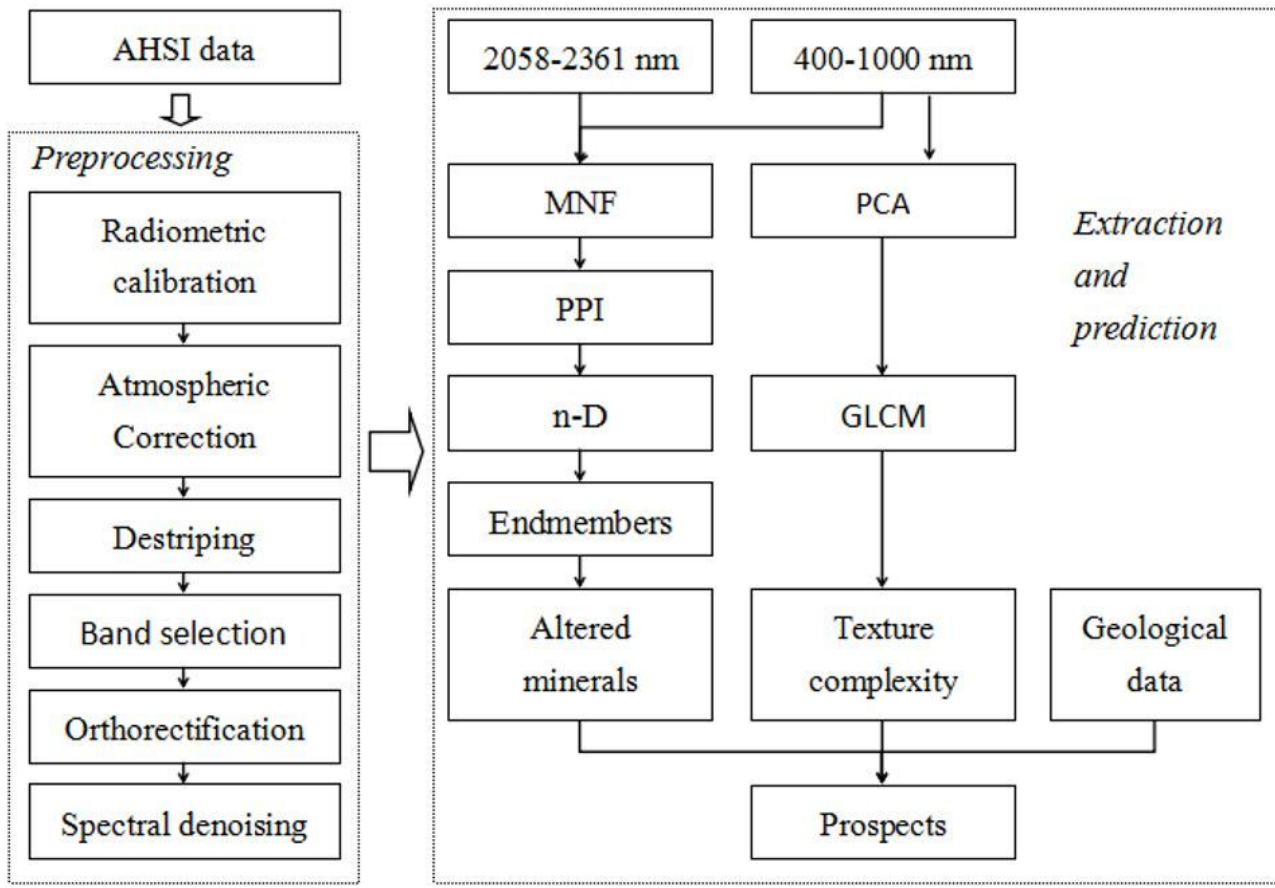


**Figure 2**

Flow diagram of the methodology.

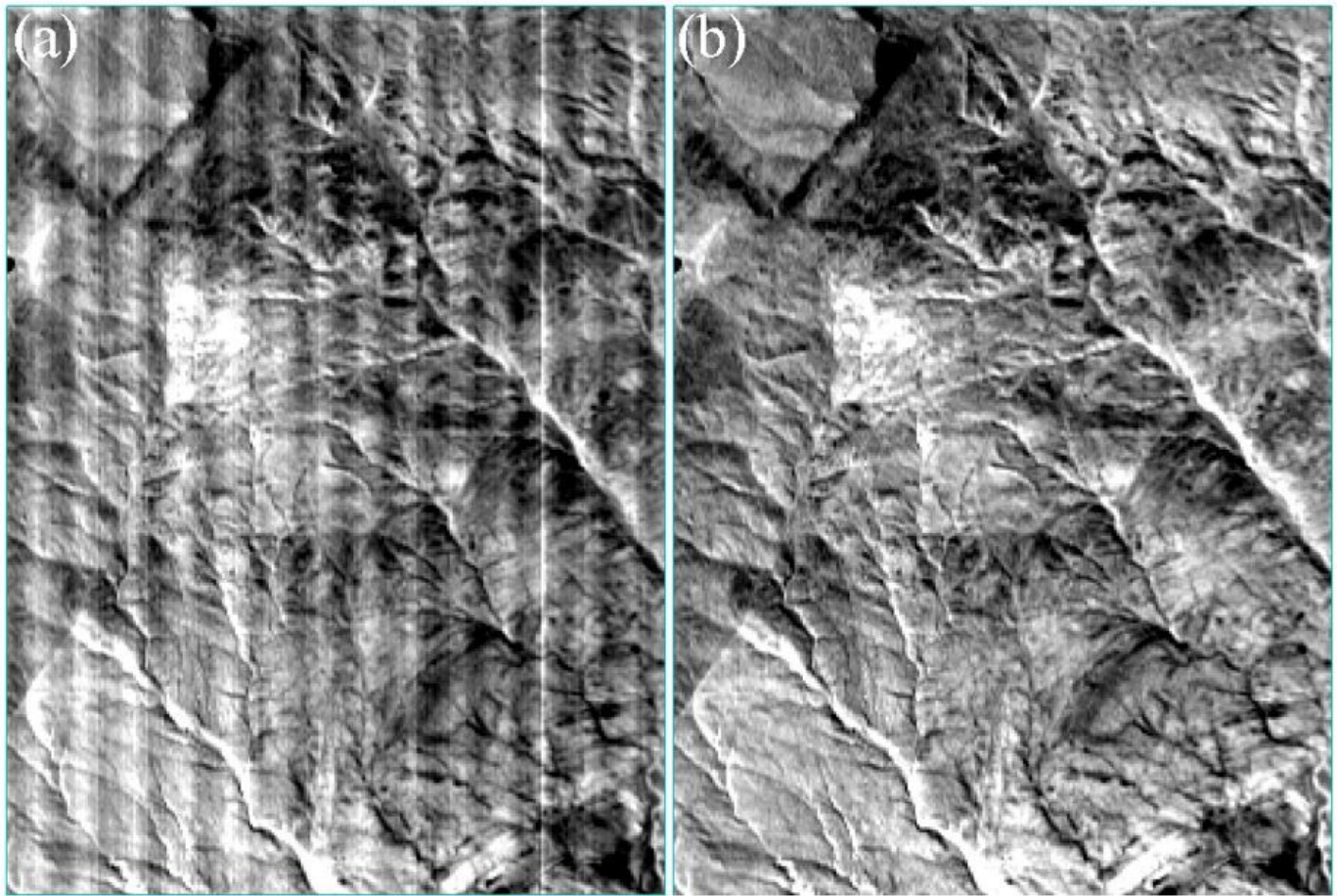


**Figure 3**

Comparison of Band 276 before (a) and after (b) destriping.

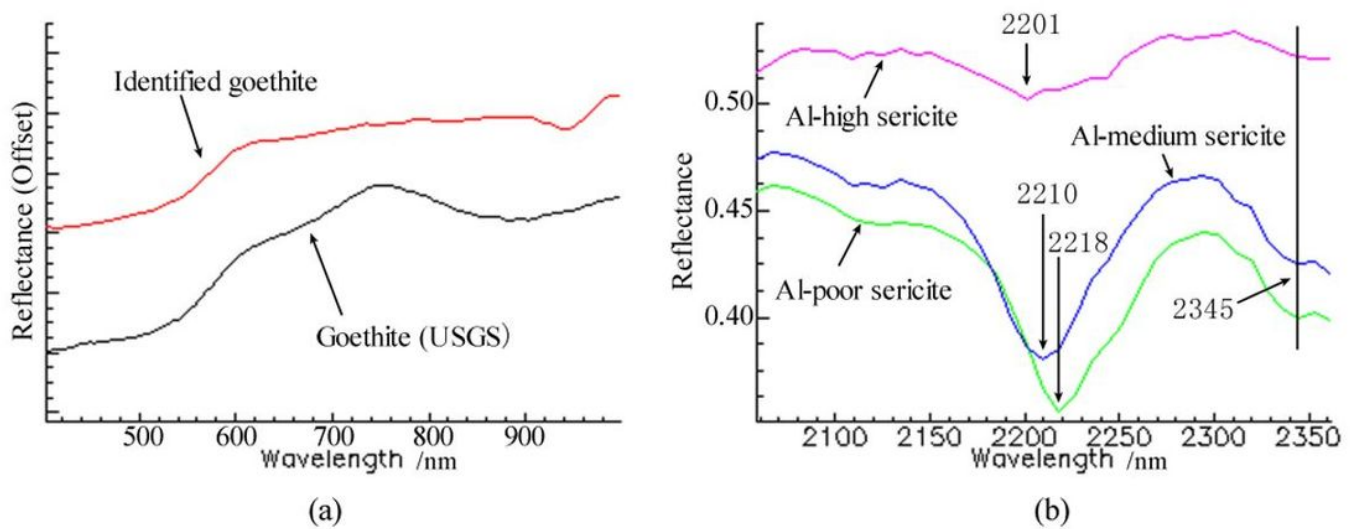


**Figure 4**

(a) Endmember spectrum in VNIR region. (b) Endmember spectra in SWIR region.

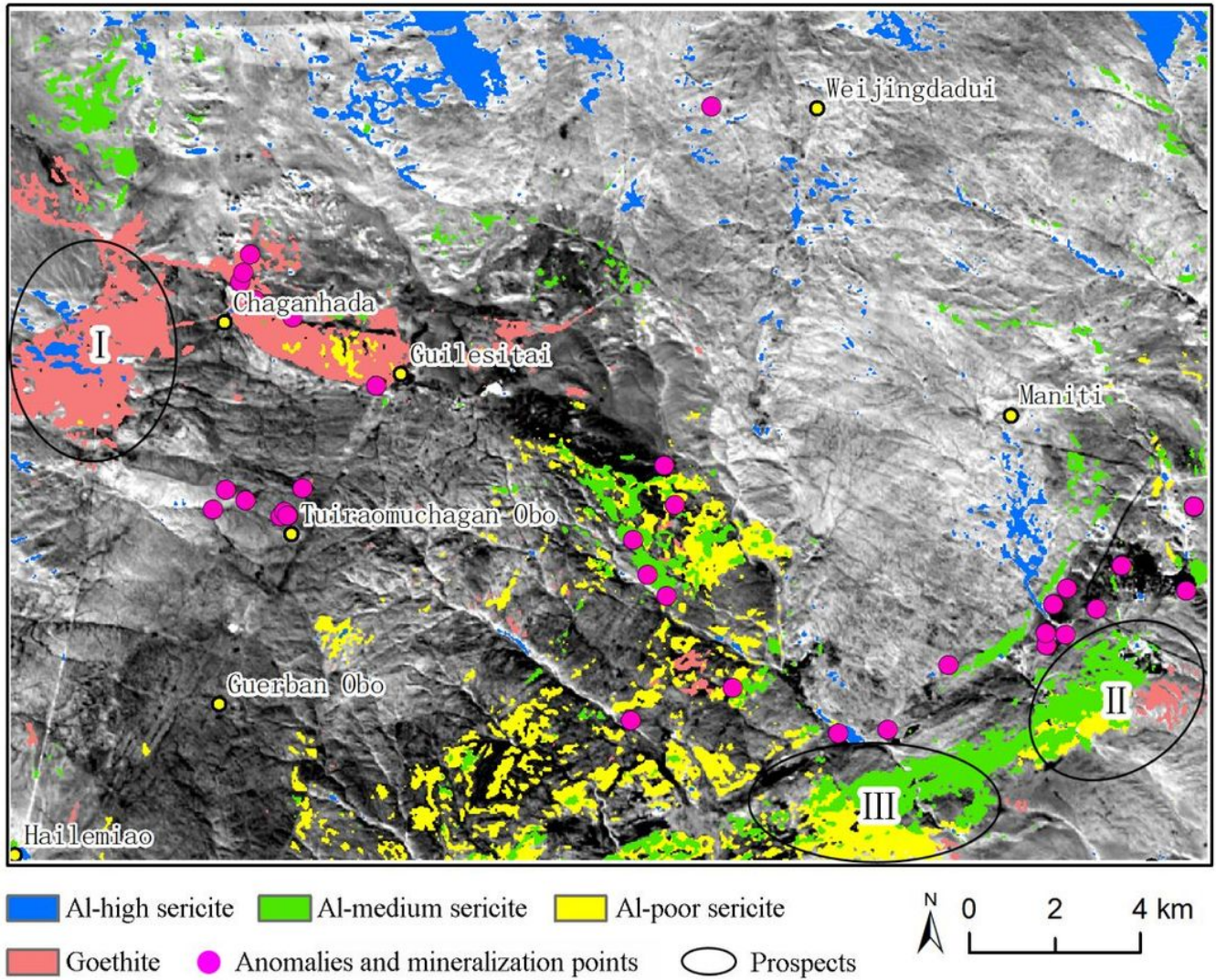


**Figure 5**

Alteration minerals and their relationship with uranium mineralization. This map was created in ESRI ArcMap 10.2 (<https://desktop.arcgis.com/zh-cn/arcmap/>).

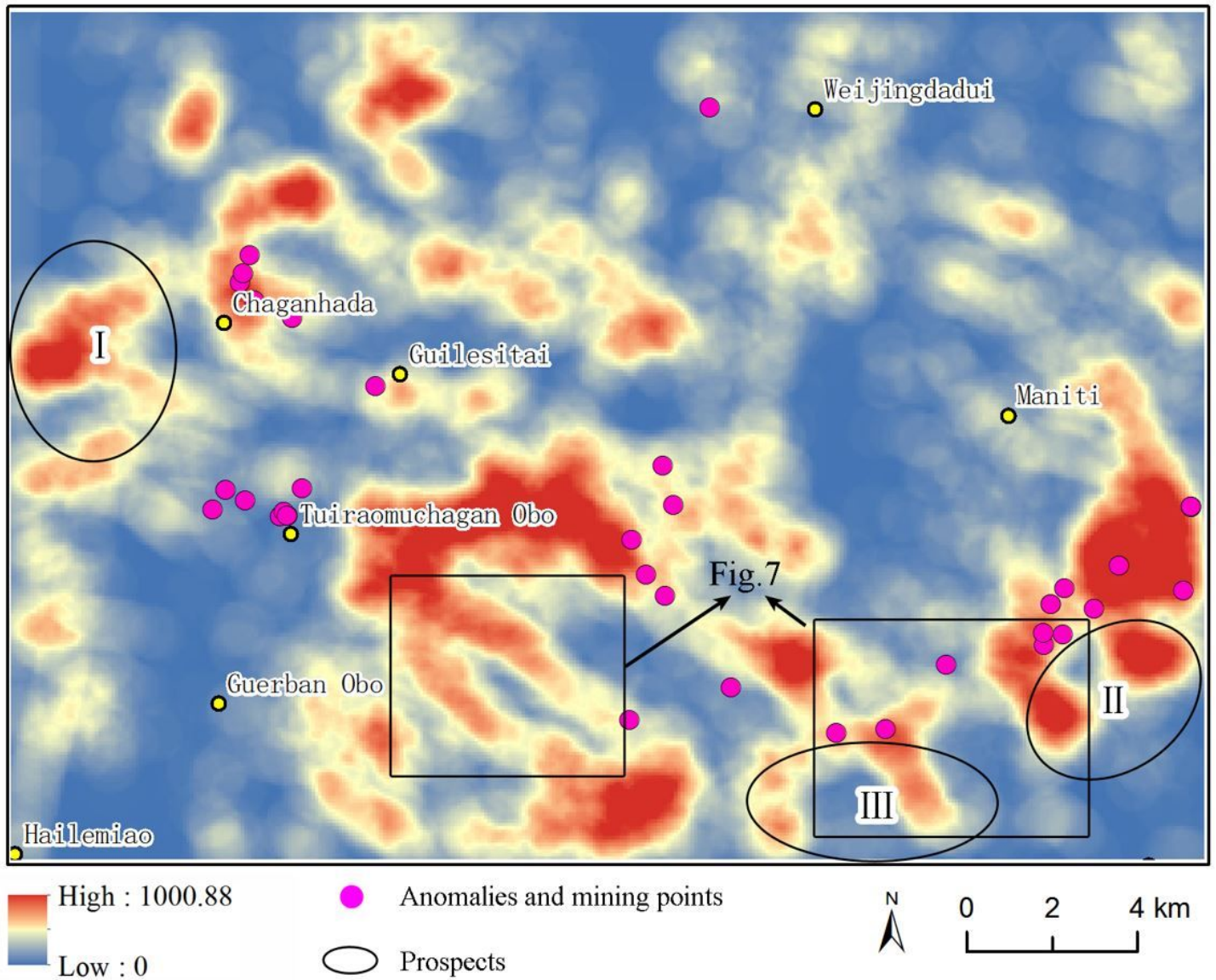


**Figure 6**

Texture complexity and its relationship with uranium mineralization. This map was created in ESRI ArcMap 10.2 (<https://desktop.arcgis.com/zh-cn/arcmap/>).

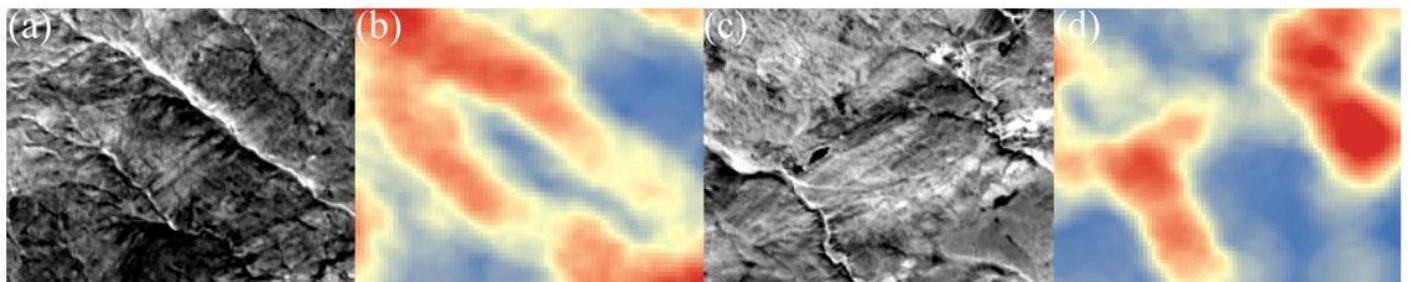


**Figure 7**

Actual images (a and b) and corresponding texture complexity (b and d).